Geometric Augmentation of Topological Track Atlas for Localization

Carsten Hasberg and Stefan Hensel
Karlsruhe Institute of Technology
Institute of Measurement and Control Systems
D-76131 Karlsruhe, Germany
{carsten.hasberg, stefan.hensel}@kit.edu

Abstract – *In automotive domain localization is typically performed through fusion of observations e.g. GPS positions and roadmaps. A transfer of these strategies to rail vehicle positioning is often impossible, because geometric track maps are not available. Key focus of this contribution is the enlargement of given topological track maps with geometric features, to enable a map-assisted rail vehicle localization based on geometric measurements. Initially we compute the optimal path within the track topology based on local track features that are measured with an eddy current sensor system. Then we process noisy INS positions and estimate the geometric shape of the map segments the measurement train has passed. Finally we augment the corresponding segments with geometric information. The proposed method is validated on real data in a real railway scenario.*

Keywords: Mapping, Estimation, Localization.

1 Introduction

In the domain of intelligent transportation systems a robust localization is always a fundamental precondition for reasonable actions within operating systems. In addition to reliable sensor measurements an efficient and precise localization is highly dependent on accurate map information and the computed vehicle position is typically passed in relation to the map.

For automotive applications commonly geometric observations, e.g. GPS positions measurements, are combined with a digital map within a map-matching step [1] [2]. In that context key business of the map is to offer transformation between the vehicle position and current observations. Based on that mapping, observation equations can be formulated and a position tracking based on incoming measurements renders possible. If a digital map is available this strategy yields precise results, even for cheap sensor configurations.

In contrast train positioning system typically rely on sensor systems mounted along the train track and offer discrete information about a rail vehicle passes by a certain position sensor. The sensor information is fused with a topological map and offers a section wise information about the current rail vehicle position. Main drawbacks are the imprecise position information and the high maintenance costs for the distributed sensor system.

To establish a basis for precise and cheap automotive localization techniques for rail vehicles we extend available topological track maps with geometric information. Compared to [3] the map extension bases on a given topological track atlas. If an assignment to a certain track segment is possible, track shape information is added to the corresponding atlas page.

The extension is realized in two main processing steps: During the first step local track features are extracted from an eddy current sensor system. Based on this features a offline reconstruction of the traveled path renders possible. Based on this path, time intervals and atlas page numbers are employed to subdivide the geometric measurements of an integrated navigation system into subsets. Within the second main step the geometric shape is estimated for each traversed segment based on these subsets .

The remainder of this paper is organized as follows: In Section 2 we describe the traveled path reconstruction based on local track features. In Section 3 we present our probabilistic strategy to estimate the local geometry. Each element of the proposed approach is validated with a real test scenario, as depicted in Section 4. Conclusion and further work are found in the last Section 5.

2 Topological Path Reconstruction

The association of time intervals to a specific track segment in a given topological map is based on a novel eddy current sensor system (ECS), which is capable to measure the rail vehicle velocity and to detect turnouts. With this, the turnout events and the estimated length

between two turnouts are subsequently used to reconstruct the driven path in an off-line map matching step.

We employ probabilistic methods to cope with noisy measurements and heavy rail conditions. In particular, hidden Markov models are employed to first detect turnouts and, in a second step, to reconstruct the driven path in an optimal way, based on the measured features, turnout detection time and corresponding track length.

2.1 Eddy Current Sensor System (ECS)

Eddy current sensors are commonly used to detect inhomogeneities in the magnetic resistance of ferromagnetic materials. The so called ECS system consists of two differential sensors in a row, separated by the distance l. The sensors are placed in a housing for electromagnetical shielding, which enables the sensor to detect all major changes in the magnetic field along the track, mainly rail clamps but also turnouts and their components.

The ECS has two measurement outputs. First is the speed, calculated with a closed loop correlator (CLC, see [4]) and a subsequent Kalman filter step (see [5] for further details).

Second output is the raw signal $s(t)$ of the sensor. On open tracks, it is mainly induced by the clamps whose equidistant spacing yields an almost periodic signal. A considerable change of the signal, mainly in amplitude, is observable when the sensor enters turnout areas, bridges or comparable regions.

2.2 Hidden Markov Models (HMMs)

HMMs are stochastic models widely used in speech processing [6], bioinformatics [7], time series analysis and other machine learning and pattern recognition fields [8]. In this contribution we propose to employ HMMs for turnout detection and an offline driven path reconstruction based on turnout events and travelled distance. HMMs are predestined to be employed for detection, given their capabilities in coping with both, variations in length, that are induced by incorrect velocity estimates, and amplitude, mainly caused by filter effects and severe bogie movements, in a given time series signal.

We adopt the notation of Rabiner [9], to describe a HMM as two staged stochastic process. A Markov chain of N possible states and initial state distribution vector $\boldsymbol{\pi}$, obeying $\sum_{i=1}^{N} \pi_i = 1$, is completely defined by its state transition probability matrix $\mathbf{A} = \{a_{ij}\}_{N\times N}$, with $\sum_j a_{ij} = 1$. a_{ij} defines the transition probability $P(q_t|q_1...q_{t-1}) = P(q_t = j|q_{t-1} = i)$ for any state q_t at time step t. A second process generates symbols of a given set at every time step, of which only the emitted series of symbols is visible depending on the states taken at every time step. This probability $P(O_t|q_t)$ is defined in the *emission matrix* $\mathbf{B} = \{b_{jk}\}_{N\times K}$, where $b_{jk} = b_j(v_k) = P(O_t = v_k|q_t = j)$ and $\sum_j b_{jk} = 1$. For both HMMs, turnout detection and map matching, continuous probability density functions according to $P(O_t = \mathbf{x}|q_t = j) = b_j(\mathbf{x})$ with $b_j(\cdot)$ obeying $\int_x b_j(\mathbf{x})d\mathbf{x} = 1$ are used.

A HMM is hence completely determined by its parameter set $\boldsymbol{\lambda} = (\boldsymbol{\pi}, \mathbf{A}, \mathbf{B})$. For further details on HMMs and their applications we refer to [10].

2.3 Turnout Detection with HMMs

The ECS signal is transformed into spatial space $s(x)$ first, using the time signal $s(t)$ and the velocity $\hat{v}(t)$ estimated by the Kalman filter. The stochastic model is built afterwards, based upon an ideal turnout shown in Figure 1, which also depicts an exemplarily ECS signal of a turnout. It illustrates the different amplitudes and shapes of the signal when passing turnouts. Each physical segment, e.g. frog, represents a state of the HMM. This allows a validation of the segmented results by evaluating the state duration and probability characteristics of the estimated *a posteriori* sequence. Afterwards, the so called signature is computed via

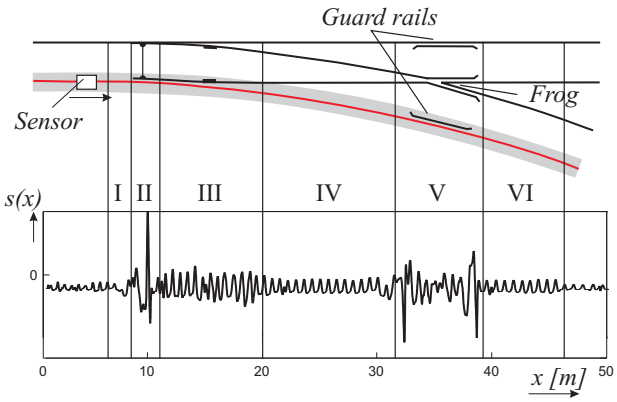

Figure 1: Scheme of a turnout and corresponding sensor signal $\tilde{r}(l)$ when driving on the right branch track.

variance calculation, exploiting the signal property of having zero mean. The mean variance corresponds to the signal power over a given integration interval, what results in a non periodic signature of length T that serves as observation sequence $\boldsymbol{\mathcal{O}}_T = \{O_1, ..., O_T\}$ for the detection-HMM. We assume Gaussian observation densities $b_i(\mathbf{x}) = \mathcal{N}(\mathbf{x}|\mu_i, \sigma_i^2)$, whose parameters are estimated with *maximum likelihood* estimates from real ECS signals. The transition probabilities and, therefore, implicitly the state durations of the HMM are modeled with the *state-tying* technique to transform the Markov chain intrinsic geometric distribution to the negative binomial distribution. Turnout parts with high discriminative character, such as guard rails or switchblades contain more sub states, while interconnecting areas are built up of few sub states to catch up with the different length of the several turnout types.

The resulting HMM consists of six sub models $\boldsymbol{\lambda}_{1..6}$ that represent the four possible turnout passing direc-

tions and two models for disturbances such as bridges or laid cables. The six models are interconnected by an additional bimodal sleeper state to enable continuous signal segmentation. Evaluation is performed with the Viterbi algorithm according to [11]. The HMM is capable of segmenting an ECS signal into turnouts, disturbances and common track areas as well as giving a classification of the driving direction. This allows to distinguish between passing turnouts facing or trailing, which is essential to determine the starting point of the turnout that determines the time of the detection event. A typical result of the segmentation algorithm for a station on a real test track is depicted in Figure 2. The red boxes indicate the segmented areas. Their height represents their type, in case of a turnout also the driving direction. Further details on signal preprocessing, turnout modeling and segmentation are given in [12]. An evaluation with real test drive data

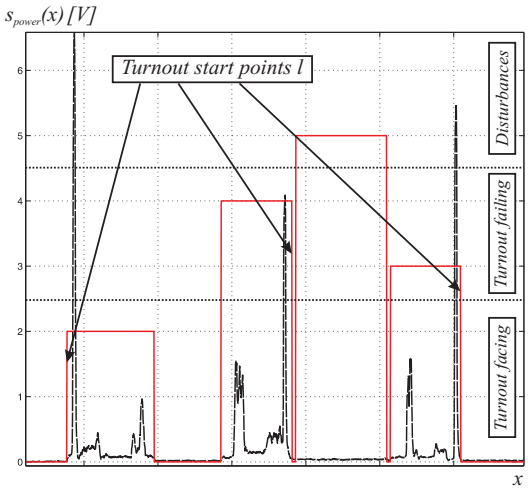

Figure 2: Turnout segmentation and classification in passing facing or trailing. Classification input is the preprocessed power signal of $s(x)$.

comprising 845 turnouts, proved an overall recognition rate of 98.34% for solely detection. From 831 properly detected turnouts 774 were positively classified in the correct driving direction when distinguished in facing and failing, corresponding to a performance of 93.14%.

2.4 Path Reconstruction with HMMs

With the described signal segmentation it is possible to measure the driven path in between two subsequently detected turnouts by integrating the estimated velocity $\hat{v}(t)$. This information is sufficient for a graph matching within a topological map to reconstruct the driven path. Assuming noisy measurements, possible misclassification of the driving direction or detection errors makes it necessary to employ the already described probabilistic methods.

2.4.1 Topological map representation

In contrary to the desired geometrical maps, topological maps are graph-based abstract representation of the environment. We interpret the turnouts as edges T and the connecting rail tracks as vertices V in a graph. This allows for a compact formulation of driving restrictions induced by turnouts. Figure 3 displays a map commonly used in signalling centers and trains. Besides the general availability, it contains information of the distances between turnouts and is enhanced with track specific features, such as road crossings or platform positions. This kind of map is sufficient to be transformed into a directed graph, represented by the adjacency matrix G. The graph deduction and segment association is depicted in detail in Figure 4.

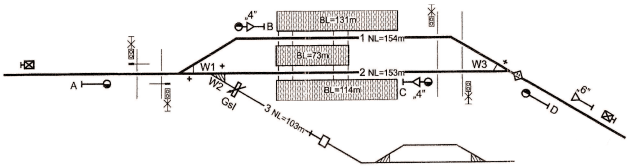

Figure 3: Topological representation of a railway station on a side track.

Each segment V_i, with $i = 1, ..., M$ is enhanced with the track length given in the topological map. The two possible driving directions on a track are coded in separate graphs and can be classified given the observation sequence.

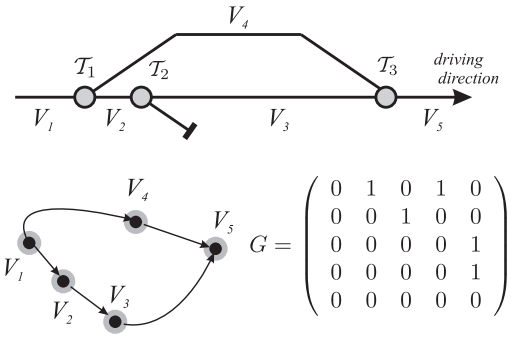

Figure 4: Deduction of the given map depicted in Figure 3 into directed graph representation.

2.4.2 Reconstruction-HMM parameter setup

The chosen setup for the construction of G leads to a special *left-right model* topology. Our topology assumes only transitions to a state higher than the current and allows no self transitions ($a_{ij} = 0 \; \forall j < i \wedge a_{ii} = 0$). The initial transition matrix $\mathbf{A}^0$ of size is $M \times M$ is directly derived from G by dividing the possible driving directions in a row through the sum of the row.

To reflect possible false negative detections, we employ an augmented linear left-right model depicted in Figure 5, which allows to compensate a missed turnout.

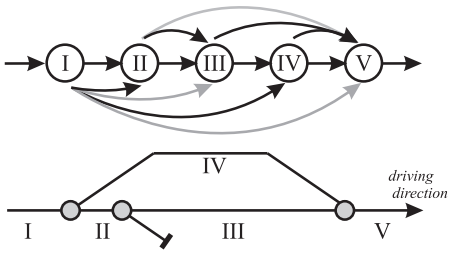

Figure 5: Applied left-right model structure without self transitions. In this model it is $a_{23} = 2 \cdot a_{25}$ and $a_{12} = a_{14} = 2 \cdot a_{13} = 2 \cdot a_{15}$ and transitions that result out of missed turnouts are kept in grey.

This is reasonable, given that two missed turnouts lead to an too uncertain path hypothesis. Therefore, we transform the initial transition matrix with the following algorithm:

Algorithm 1 Calculation of transition probabilities a_{ij}

```
for i = 1 to M-1 do
  for j = 1 to M do
    if α_ij > 0 then
      n++
      α_ij = 2
    end if
    if α_(i+1)j > 0 then
      m++
      α_ij = 1
    end if
  end for
  for j = 1 to N do
    α_ij = α_ij/(2 · n + m)
  end for
end for
```

This algorithm assigns a double weight to favor direct connections compared to the *left one out* probabilities to create the final transition matrix $\mathbf{A}$.

For each segment i, we assume a Gaussian distributed uncertainty of the segment length $l_{\text{seg}}(i)$, with a deviation $\hat{\sigma}_{seg}$ proportional to the segment length. The segment length is directly taken out of given maps as depicted in Figure 3. The probability density function (pdf) for the length of an HMM-state/segment i thus becomes for an individual segment

$$p_{ii}(\mathbf{x}) = \mathcal{N}(\mathbf{x}|l_{\text{seg}}(i), \hat{\sigma}^2_{\text{seg}}(i)), \tag{1}$$

given $\hat{\sigma}_{\text{seg}}(i) = l_{\text{seg}}(i) \cdot \kappa$. Missed turnouts lead to an additive combination of two segments, resulting in the pdf

$$p_{ij}(\mathbf{x}) = \mathcal{N}(\mathbf{x}|l_{\text{seg}}(i) + l_{\text{seg}}(j), \hat{\sigma}^2_{\text{seg}}(i,j)) \tag{2}$$

given $\hat{\sigma}_{\text{seg}}(i,j) = (l_{\text{seg}}(i) + l_{\text{seg}}(j)) \cdot \kappa$, where in both cases, $\kappa \in [0,1]$.

All over, the emission density for each state becomes a Gaussian mixture defined as

$$b_i(\mathbf{x}) = c_{ii}\, p_{ii}(\mathbf{x}) + \sum_{j}^{R} c_{ij}\, p_{ij}(\mathbf{x}), \tag{3}$$

where R is the number of connections from state i in $\mathbf{A}^0$ and $c_{ij} = c_{ii} = \frac{1}{R+1}$.

2.4.3 Viterbi based sequence classification

In this contribution, the inferred state sequence $q^*(t)$ of the second HMM represents physical entities, the rail network segments, and is therefore of special interest.

The observation sequence $\boldsymbol{\mathcal{O}}_T$ consists of distances $\hat{d}_{k,k+1}$ between two turnout events at time t_k and t_{k+1}, starting with the first detection, and is

$$O_{t+1} = \hat{d}_{k,k+1} = \int_{t_k}^{t_{k+1}} \hat{v}(t)dt, \tag{4}$$

with the Kalman filter velocity estimate $\hat{v}(t)$. We apply the *min-sum* or Viterbi algorithm [11] to decode the HMM in an optimal way, with respect to *block error rate*. Figure 6 depicts an exemplarily situation, where for a simulated rail network the observation sequence are at first undisturbed $\mathbf{l}_{\text{seg}}$. the second sequence simulates a missed turnout.

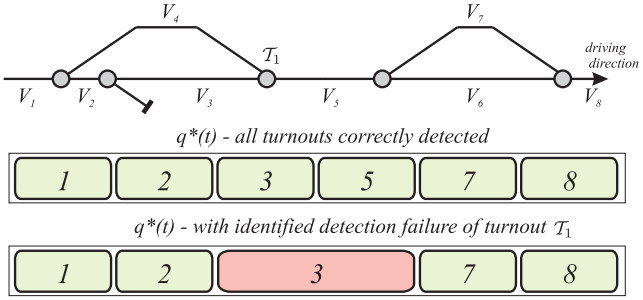

Figure 6: Inferred sequence $q^*(t)$ for two different $\boldsymbol{\mathcal{O}}_T$, simulating a missed turnout.

The second run is still usable to create geometric map features for the segments $1, 2, 7$ and 8, in spite of a missed turnout.

After the most probable sequence $q^*(t)$ was determined, the HMM is used for further result verification. The likelihood $\mathcal{L}_{HMM}$ given $q^*(t)$ and $\boldsymbol{\lambda}$ is calculated with the forward probabilities [9]. We calculate the *log-odds* [7] instead of $\mathcal{L}_{HMM}$ to compensate for varying lengths in $\boldsymbol{\mathcal{O}}$, to enable the comparison of test drives with and without missed turnouts. This allows to set a threshold $\xi_{\min}$ beyond which the path is rejected for further geometric map building steps. This ensures that only correct reconstructed paths with reliable information are used for further geometric estimation.

3 Bayesian Mapping

Applying the results from Section 2 we can subdivide the geometric measurements and assign them to the corresponding atlas pages. We extend our concept of Probabilistic Road Maps (PRM) [13] to model rail tracks. Because there is no prior knowledge about the geometric characteristics of a certain rail segment available the model complexity can not be set in advance and the optimal number of model parameters has to be selected. Given observations on the one hand and a set of possible models on the other hand, the estimation of the model parameters and the comparison of different models is accomplished with Bayesian methods. Detailed descriptions can be found in [8] and [14]. Due to the linear relationship between model parameters and model predictions approximation free inference renders possible.

3.1 Sensor System

An integrated navigation system is mounted in the gravity center of a the test vehicle. It consists of two main components: The first component is a dead-reckoning inertial navigation system (INS). Altogether it contains six sensors, namely three accelerometers and and three gyroscopes, that measure acceleration and rotational rate of the vehicle. The second component is a GPS receiver to cope with the unbounded growing position drift of the INS. Typically, GPS aided INS navigation is called integrated navigation [15]. For details about the underlying principles and algorithms see [16].

The position estimate $\mathbf{z}_n$ at time t_n is part of the navigation solution and is converted to Universal Transverse Mercator (UTM) coordinate system, a two dimensional Cartesian coordinate system [16]. Additionally we obtain high precise information about the distance traveled l_n from the ECS system for each position measurement.

3.2 Probabilistic Road Map

The concept of Probabilistic Road Maps bases on prior knowledge about road or track construction rules that are commonly composed of a sequence of geometric primitives to enable a comfortable driving without any abrupt variations in lateral acceleration. Unlike current realizations of road-constrained motion tracking algorithms that often base on polygonal models we chose smooth third order spline curves. Especially in case of curved roads this modelling strategy overcomes systematic interpolation errors and yields precise approximation results, both for strong curved roads and straight road sections. Based on an arc-length curve parameterization a close measurement-to-curve relationship renders possible.

Cubic spline interpolation [17] is chosen to approximate motion constraints. The interpolation is carried out stepwise based on a given set of supporting points

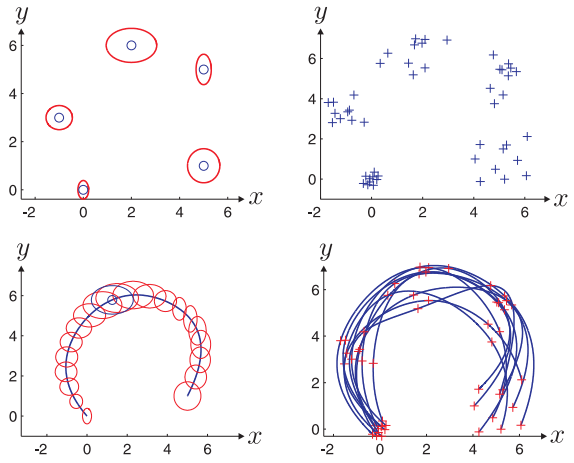

Figure 7: Probabilistic interpolation with planar, global cubic spline curves

$\mathbf{p}_i = (p_{x,i}, p_{y,i})$ for $i = 1, \ldots, M$. In particular, each geometric segment is interpolated with a planar curve

$$\mathbf{s}(l) = \begin{bmatrix} a_{x,i} + b_{x,i}\Delta l_i + c_{x,i}\Delta l_i^2 + d_{x,i}\Delta l_i^3 \\ a_{y,i} + b_{y,i}\Delta l_i + c_{y,i}\Delta l_i^2 + d_{y,i}\Delta l_i^3 \end{bmatrix}, \tag{5}$$

with l denoting arc length and with $\Delta l_i = l - l_i$. The process of parameter calculation can be formulated as

$$\mathbf{s}(l) = \mathbf{G}(l)\mathbf{x} \tag{6}$$

where all polynomial coefficients are subsumed in

$$\mathbf{x} = [p_{x,1}, \ldots, p_{x,M}, p_{y,1}, \ldots, p_{y,M}]^T. \tag{7}$$

We integrate continuous available geometrical uncertainty of function $\mathbf{s}(l)$ in a multivariate probability distribution of the supporting point vector $\mathbf{x}$ within the generative model (6). The resulting probabilistic model maps the chosen distribution onto the model output. The uncertainty of $\mathbf{x}$ is given by $\mathcal{N}(\mathbf{x}|\mu_\mathbf{x}, \mathbf{\Sigma}_\mathbf{x})$ and propagates through equation (6) to the planar spline curve $\mathbf{s}(l)$. Figure 7 depicts the distributions of the supporting point vector and the corresponding spline curve as well as 10 realizations.

3.3 Parameter Estimation

Initially the available data $\mathcal{D}$, that contains N position observations $\mathbf{z}_n$ of the curve for given curve length l_n are grouped together in the random vector $\mathbf{z} = [\mathbf{z}_1, \ldots, \mathbf{z}_N]^T$. Further more we assume $\mathbf{z}$ to be a normal distributed random variable with known covariance $\mathbf{\Sigma}_\mathbf{z} = \beta^{-1}\mathbf{I}_{2N}$.

The Likelihood function of the parameter can be deduced from the probabilistic model of the splines presented in Section 3.2. According to (6) a linear relation between the function value $\mathbf{s}(l)$ and the supporting point vector $\mathbf{x}$ is given. Using this mapping and and an

additive noise terme $= [\mathbf{e}_1, \ldots, \mathbf{e}_N]^T$ the observations $\mathbf{z}$ can be explained within an linear observation model

$$\mathbf{z} + \mathbf{e} = \begin{bmatrix} \mathbf{s}(l_1) \\ \vdots \\ \mathbf{s}(l_N) \end{bmatrix} = \begin{bmatrix} \mathbf{G}(l_1) \\ \vdots \\ \mathbf{G}(l_N) \end{bmatrix} \mathbf{x} =: \mathbf{H}\mathbf{x} \tag{8}$$

The coefficients of matrix $\mathbf{H}$ are known and only depend upon the input variables l_n.

Based on the assumption of a normal distributed observation vector $\mathbf{z}$ the likelihood function follows directly

$$p(\mathbf{z}|\mathbf{x}) = \mathcal{N}(\mathbf{H}\mathbf{x}, \Sigma_{\mathbf{z}}) = \mathcal{N}(\mathbf{H}\mathbf{x}, \beta^{-1}\mathbf{I}_{2N}) \tag{9}$$

If the model parameters $\mathbf{x}$ are known this relationship explains the expected observation as a linear transformation of the model parameters.

We presume to have prior knowledge about the unknown model parameter $\mathbf{x}$. In contrast to polynomial coefficients a prediction of the actual supporting point values of the piecewise defined splines is easier. In particular if rough information about the area that should be mapped is available we can specify domains in x and y coordinates the parameter values lie within and approximate this equal distributed prior with a normal distribution, due to its computational advantages. Due to clarity the prior density is

$$p(\mathbf{x}) = \mathcal{N}(\mathbf{x}|\mu_{\mathbf{x}}, \Sigma_{\mathbf{x}}) = \mathcal{N}(\mathbf{x}|\mathbf{0}, \alpha^{-1}\mathbf{I}_{2M}) \tag{10}$$

for M spline supporting point and therefore $2M$ parameters. The handling of more general normal distributions is equal in the essential processing steps.

Next step is to calculate the posterior density, that is proportional to the product of the likelihood function (9) and the prior density (10). Due to the conjugate prior the posterior is also Gaussian. Completing the square and normalize the result gives [14]

$$p(\mathbf{x}|\mathbf{z}) = \mathcal{N}(\mathbf{x}|\mu_{\mathbf{x}|\mathbf{z}}, \mathbf{\Sigma}_{\mathbf{x}|\mathbf{z}}) \tag{11}$$

with

$$\mu_{\mathbf{x}|\mathbf{z}} = \beta\mathbf{\Sigma}_{\mathbf{x}|\mathbf{z}}\mathbf{H}^T\mathbf{z} \tag{12}$$

$$\mathbf{\Sigma}_{\mathbf{x}|\mathbf{z}} = \left(\beta\mathbf{H}^T\mathbf{H} + \alpha\mathbf{I}_{2M}\right)^{-1}. \tag{13}$$

3.4 Model Prediction

Actually we are not interested in the parameter values $\mathbf{x}$ itself but in prediction of unobserved curve positions $\mathbf{z}_l$ for new arc length values l within the interval $l_1 \leq l \leq l_N$. Marginalize over the supporting points gives

$$p(\mathbf{z}_l|\mathbf{z}) = \int p(\mathbf{z}_l|\mathbf{x})p(\mathbf{x}|\mathbf{z})d\mathbf{x} \tag{14}$$

$$= \int \mathcal{N}(\mathbf{z}_l|\mathbf{G}(l)\mathbf{x}, \beta^{-1}\mathbf{I}_2)p(\mathbf{x}|\mathbf{z})d\mathbf{x}. \tag{15}$$

The convolution of two normal distributed random variables yields again a Gaussian density, with

$$p(\mathbf{z}_l|\mathbf{z}) = \mathcal{N}(\mathbf{z}_l|\mathbf{G}(l)\mu_{\mathbf{x}|\mathbf{z}}, \mathbf{\Sigma}_{\mathbf{z}_l|\mathbf{z}}) \tag{16}$$

with

$$\mathbf{\Sigma}_{\mathbf{z}_l|\mathbf{z}} = \mathbf{G}(l)\mathbf{\Sigma}_{\mathbf{x}|\mathbf{z}}\mathbf{G}(l)^T + \beta^{-1}\mathbf{I}_2. \tag{17}$$

While the fist term of the covariance subsumes the prediction uncertainty caused by the parameter estimation, the second term describes the noise of the observations.

3.5 Model Selection

The task is now to chose the model, within the finite set of possible models, that enables the best predictions. Therefore we interpret each corresponding model $\mathcal{M}_i$ as a hypothesis about the process that generates the observations $\mathbf{z}$. The particular number of supporting points M per set of observations can be varied and we have to decide which one to take.

Analogue to the parameter estimation procedure the decision bases on the theorem of Bayes

$$p(\mathcal{M}_i|\mathbf{z}) \sim p(\mathbf{z}|\mathcal{M}_i)p(\mathcal{M}_i). \tag{18}$$

While there is no prior knowledge about the hypothesis available the prior density $p(\mathcal{M}_i)$ is equal for all possible hypothesis. Hence, the posterior density $p(\mathcal{M}_i|\mathbf{z})$ is proportional to the evidence. As a consequence the evidence

$$p(\mathbf{z}|\mathcal{M}_i) = \int p(\mathbf{z}|\mathbf{x}, \mathcal{M}_i)p(\mathbf{x}|\mathcal{M}_i)d\mathbf{x}. \tag{19}$$

can be used to evaluate the relative performance of different models. Because the likelihood and the prior density are Gaussians the unknown marginal distribution is also Gaussian and the evidence (19) for a model $\mathcal{M}$ is

$$p(\mathbf{z}|\mathcal{M}) = \mathcal{N}(\mathbf{z}|\mathbf{0}, \alpha^{-1}\mathbf{H}\mathbf{H}^T + \beta^{-1}\mathbf{I}_{2N}) \tag{20}$$

Finally the model with the highest evidence is chosen. Making use of the monotony of the log function one can calculate

$$\ln p(\mathbf{z}|\mathcal{M}) = -N\ln(2\pi) - \frac{1}{2}\ln|\alpha^{-1}\mathbf{H}\mathbf{H}^T + \beta^{-1}\mathbf{I}_{2N}| - \frac{1}{2}\mathbf{z}^T(\alpha^{-1}\mathbf{H}\mathbf{H}^T + \beta^{-1}\mathbf{I}_{2N})^{-1}\mathbf{z} \tag{21}$$

Maximizing the log evidence

$$\mathcal{M}_{MAP} = \arg\max_{\mathcal{M}_i} \ln p(\mathbf{z}|\mathcal{M}_i). \tag{22}$$

gives the most likely model.

3.6 Example

We applied the Bayesian strategy to the PRM. The task is to estimate the planar curve in Figure 8. Initially 30 curve parameter values are drawn from an equal distribution along the total curve length. Then an additive Gaussian white noise term with the covariance $\beta^{-1} = 1.5 \cdot 10^1$ is added to generate the available observations.

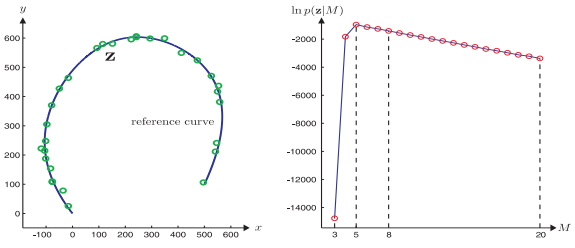

Figure 8: Left: Reference curve and available 30 observations. Right: Log evidence against the used number of supporting points.

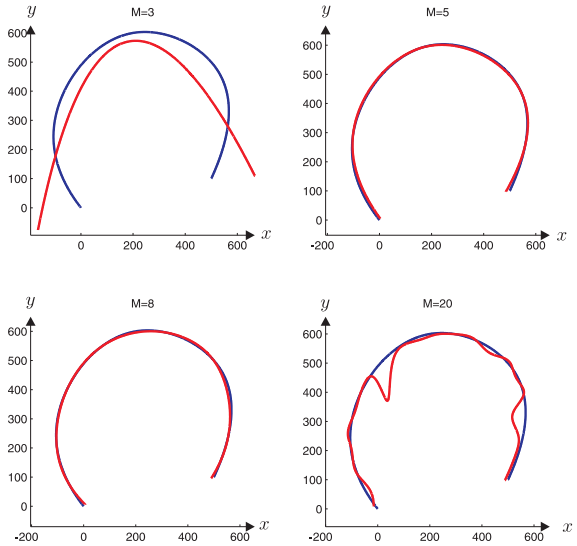

Figure 9: Estimated maximum posteriori planar curve progression $\hat{\mathbf{s}}_{MAP}(l) = \mathbf{G}(l)\hat{\mathbf{x}}_{MAP}$ for different models that differ in the number of available supporting points against the reference curve.

The prior density of the model parameters is assumed to be a zero mean normal distribution with a covariance $\alpha^{-1}\mathbf{I}_{2M}$ with $\alpha = 1.0 \cdot 10^{-3}$. In Figure 8 the model evidence is plotted against the number of basis functions. Together with Figure 9 the progression of the evidence for an increasing number of basis functions is comprehensible: For $M = 3$ the quality of the model to predict the observed data is inadequate, hence the evidence value is very small. For a number of $M = 5$ supporting points the approximation of the reference shape is much better and precise predictions based on this model are possible. Further increasing of model complexity does not cause better predictions, hence the model evidence decreases for $M > 5$. Oszillation behavior can be observed for $M = 20$.

4 Experimental Results

Several test drives were conducted to verify the approach with real data. The test track is situated in a valley and is mainly built up of a one track line, splitting up in the train stations. It is half situated in wooded area that additionally reduces the GNSS accuracy. Starting point is a two track part up to the first station. The total length of the track is 18.45 km with a reversing track loop at the end station. Test vehicle is a common tram used in daily traffic. A highly precise digital map exists for the whole track, which is used as ground truth for verification purposes.

The evaluation for the topological path reconstruction comprises of 10 labeled test drives for a side track area with 5 stations and 13 turnouts. For the given data, all turnouts were correctly detected and the path successfully reconstructed. The *log-odds* for a correct path were determined to be above $\xi_{\text{cor}} = -40$. Simulated miss detections resulted in a comparable value. Further missing detections or artificially disturbed distance measurements result in a *log-odds* threshold for rejection determined to $\xi_{\text{min}} = -110$.

We subdivided the INS data sets based on the traveled path and estimated the geometric models for each atlas page. While velocities in between stations are typically higher less data per distance traveled is collected. For these kind of tracks the Bayesian model selection typically favors a model with one supporting point per $50 - 80$m. An example is visualized in Figure 10. For station scenarios more data is available and we end up with a distance between supporting points in between 10m and 30m. An example is depicted in Figure 10. Due to the precise INS navigation solution the overall accuracy is, compared to the reference map always better than $1.5m$.

5 Summary and Conclusions

To establish a basis for precise and cheap automotive localization techniques for rail vehicles we extend available topological track maps with geometric information. The map extension bases on a given topological track atlas and is realized in two main processing steps. During the first stage local track features are detected and an offline reconstruction of the traveled path renders possible. In the second stage the shape of each atlas page is estimated. In particular cubic spline are employed and model selection and parameter estimation is performed based on global track position measurements. The proposed approach is validated within a real side track scenario. Future work will focus on the adaption of automotive localization techniques to enhance current train positioning systems.

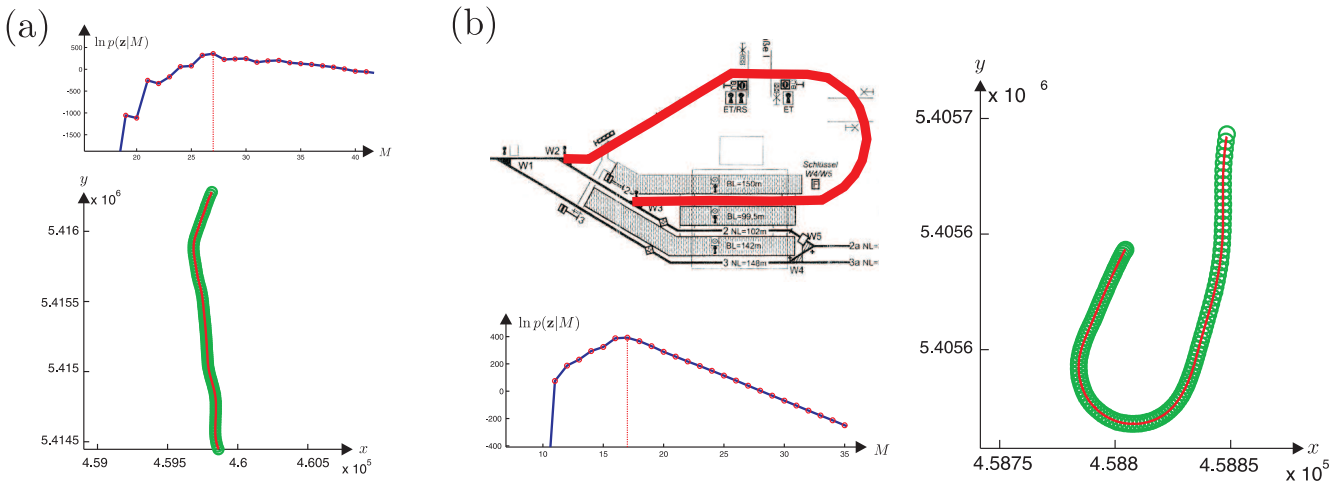

Figure 10: Scenario (a) Top: Maximum of $\ln p(\mathbf{z}|M)$ for model with $M = 27$ supporting points. Bottom: Position observations (green) and estimated curve (red). Due to the total curve length of 1875m the distance between adjacent supporting points is 1875m/27 = 69.44m. Scenario (b) Left: Topological map and chosen segment (red) and maximum of $\ln p(\mathbf{z}|M)$ for model with $M = 17$ supporting points. Right: Corresponding observations (green) and estimated curve (red). Due to the total curve length of 286m the distance between adjacent supporting points is 286m/17 = 16.82m.

References

[1] M. A. Quddus, W. Y. Ochieng, and R. B. Noland, "Current map-matching algorithms for transport applications: State-of-the art and future research directions," *Transportation Research Part C, Elsevier*, vol. 15, pp. 312 – 328, 2007.

[2] I. Skog and P. Händel, "In-Car Positioning and Navigation Technologies - A Survey," *IEEE Transactions on Intelligent Transportation Systems*, vol. 10, pp. 4–21, 2009.

[3] S. Hensel and C. Hasberg, "Multi sensor mapping of rail networks," in *Proc. of the 12th IEEE International Conference on Information Fusion, 2009*, 2009.

[4] T. Engelberg and F. Mesch, "Eddy current sensor system for non-contact speed and distance measurement of rail vehicles," in *Computers in Railways VII*, pp. 1261–1270, WIT Press, 2000.

[5] T. Strauss, C. Hasberg, and S. Hensel, "Correlation based velocity estimation during accelaration phases with application in rail vehicles," in *IEEE/SP 15th Workshop on Statistical Signal Processing*, 2009.

[6] J. Bilmes, "What HMMs can do," tech. rep., University of Washington, 2002.

[7] R. Durbin, *Biological sequence analysis*. Cambridge University Press, 2002.

[8] D. MacKay, *Information Theory, Inference and Learning Algorithms*. Cambridge University Press, 2003.

[9] L. Rabiner, "A tutorial on hidden Markov models and selected applications in speech recognition," *Proceedings of the IEEE*, vol. 77, pp. 257–286, 1989.

[10] Y. Ephraim and N. Merhav, "Hidden markov processes," *IEEE Transactions on Information Theory*, vol. 48, pp. 1518 – 1569, June 2002.

[11] A. Viterbi, "Error bounds for convolutional codes and an asymptotically optimum decoding algorithm," *IEEE Transactions on Information Theory*, vol. 5, pp. 260–269, 1967.

[12] S. Hensel and C. Hasberg, "HMM based segmentation of continuous eddy current sensor signals," in *Proc. IEEE International Conference on Intelligent Transportation Systems*, pp. 760 – 765, 2008.

[13] C. Hasberg, "Regression with probabilistic cubic splines," in *Robotics Science and Systems (RSS) Workshop on Regression in Robotics*, 2009.

[14] C. Bishop, *Pattern Recognition and Machine Learning*. Information Science and Statistics, 2006.

[15] Y. Bar-Shalom, X. Li, and T. Kirubarajan, *Estimation with Applications to Tracking and Navigation: Theory, Algorithms and Software*. John Whiley and Sons, 2001.

[16] D. Titterton and J. Weston, *Strapdown Inertial Navigation Technology*, vol. 207. Reston: American Institute of Aeronautics and Astronautics, 2 ed., 2004.

[17] G. Farin, *Curves and Surfaces for CAGD*. Morgan Kaufmann, 2002.